Pergamon

Int. J. Solids Structures Vol. 32, No. 6/7, pp. 957–978, 1995

0020-7683/95 $9.50 + .00

0020-7683(94)00171-5

TOUGHENING MECHANISMS IN MIXED-MODE INTERFACIAL FRACTURE

Y.-M. LIANG and K. M. LIECHTI

Engineering Mechanics Research Laboratory, Department of Aerospace Engineering and Engineering Mechanics, The University of Texas at Austin, Austin, TX 78712, U.S.A.

(*Received* 15 *December* 1993; *in revised form* 26 *May* 1994)

Abstract—A series of mixed-mode interfacial crack initiation experiments were conducted using thinner glass/epoxy specimens than had been used in the past [Liechti and Chai (1992, *J. Appl. Mech.* **59**, 295–304)]. Three-dimensional effects were eliminated in the sense that the crack front shapes were the same for all mode-mixes. Nonetheless, the thinner specimens were associated with an overall increase in toughness and a noticeable change in the distribution of toughness with mode-mix. Interferometric measurements of normal crack opening displacements (NCOD) revealed values that were lower than predictions based on rate independent and dependent plasticity and even elastic analyses. The lower NCOD were attributed to long range cohesive crack face tractions, possibly due to electrostatic effects. Shielding calculations suggested that the long range tractions were more important than plastic dissipation. Nonetheless, they did not fully explain the shear-induced toughness effect that has been noted for this and other interfaces.

1. INTRODUCTION

The renewed interest in mixed-mode interfacial fracture mechanics that arose in the late 1980s has, among other issues, led to the development of a broader database of toughness values. Earlier indications that interfacial toughness could be a function of mode-mix have been strengthened through an exploration of more material systems and wider mode-mix ranges. Toughness values that increased with larger amounts of mode II loading were initially obtained from material combinations that involved a polymeric component (Liechti and Hanson, 1988; Cao and Evans, 1989; Thouless, 1990; Wang and Suo, 1990; Liechti and Chai, 1992; Liechti and Liang, 1992). However, alumina/niobium (O'Dowd *et al.*, 1991) and silica/copper (Thurston and Zehnder, 1993) interfaces have also exhibited the shear-induced toughening effect.

Recently, the emphasis has shifted naturally from determining toughness values in a largely phenomenological manner to developing an understanding of the mechanisms involved so that, eventually, it may be possible to predict the toughening effect. Perhaps the earliest example of this trend was the work by Evans and Hutchinson (1989) in their examination of asperity shielding. This was followed by observations (Liechti and Chai, 1992) that, although small scale yielding applied for all mode-mixes, the plastic zone sizes for a glass/epoxy interface under shear were up to two orders of magnitude higher. However, initial estimates, albeit based on stationary crack analyses, suggested that dissipation by plastic deformation did not give rise to the extent of toughening that had been measured. Nonetheless, the possibility of toughening by plastic dissipation has been maintained by the recent analysis of Tvergaard and Hutchinson (1992b) where the interface was represented by its own traction/separation law, thus allowing steady state toughness values to be extracted from growing crack analyses for a wide range of prescribed mode-mixes. The degree of toughening with shear and the toughness distribution itself agreed qualitatively with the experimental results of Liechti and Chai (1992). A direct comparison essentially awaits a mechanical characterization of the so-called interphase region (Sharpe, 1972). In this respect, it should be noted that the exact distribution of the traction/separation law for the interface or interphase region is not necessarily required (Tvergaard and Hutchinson, 1992); knowledge of the maximum stress level $\hat{\sigma}$ and the intrinsic adhesion Γ_0 will suffice.

Plastic dissipation in blister specimens (Liechti and Hanson, 1988; Liechti and Liang, 1992) was greatly enhanced because the plastic zones were elongated behind the crack front due to the peeling nature of the load introduction. When the epoxy layer was sandwiched between glass and aluminum (Liechti and Liang, 1992), plastic zones were as much as five times the sandwich layer thickness, clearly violating small scale yielding assumptions. These results and a recent examination of various blister test configurations (Liechti and Shirani, 1994) have strong implications for the use of blister tests in determining the interfacial toughness of microelectronic structures.

Another fracture mechanism that gives rise to shear-induced toughening is that interfacial separation is controlled by the stress component normal to the interface reaching the decohesion stress (O'Dowd *et al.*, 1991). However, the criterion did not yield a toughness vs mode-mix distribution that matched the data for the alumina/niobium interface, even when plastic deformations were accounted for. The rise in toughness with increasing shear, which was quite sharp, occurred at lower phase angles than had been observed in the cases involving polymeric materials. The same was true for the silica/copper interface (Thurston and Zehnder, 1993).

A potential shielding mechanism that will be considered further in this paper is the possibility of relatively long range cohesive tractions due to electrostatic effects. These have been noted both following interfacial fracture (Zimmerman *et al.*, 1991) and interfacial contact (Horn and Smith, 1992). In their study of the pullout of a steel rod from an epoxy matrix, Zimmerman *et al.* (1991) made measurements of the load and strain in the rod which were complemented by current, photon emission and radio emission measurements. Considerable responses were noted in all the complementary measurements at the onset of crack initiation, thus indicating electrostatic activity. Horn and Smith (1992) considered the non sliding contact between mica and silica in an atomic force microscope and found that an attractive force developed during contact, resulting in a noticeable adherence between the two surfaces when the applied loads were reversed. Electrostatic effects were used to explain the development of the attractive stresses which gave rise to a degree of adhesion of about 6 J/m^2, which is comparable to the toughness of a glass/epoxy interface at a mode-mix phase angle of zero. Since the shear-dominant mode-mixes that were considered in the experiments by Liechti and Chai (1992) gave rise to crack face contact, the association is close at hand that electrostatic cohesive stresses may have been generated across the crack faces both as a result of crack growth and crack face contact.†

The objective of this study was to examine the role of various potential mechanisms for the shear-induced toughening of interfaces. Experiments involving a single specimen subjected to biaxial loading with measurements of normal crack opening displacements (NCOD) near the crack front were used in conjunction with finite element analyses to examine three-dimensional effects, rate dependent plasticity and electrostatic effects.

2. INTERFACE FRACTURE EXPERIMENTS

The specimen that was used in the study was the same edge-cracked bimaterial strip (Fig. 1) under biaxial loading that was analysed and used to generate interfacial fracture data (Liechti and Chai, 1991, 1992). The thickness of the specimens was decreased from the 6.35 mm in earlier work to 2.00 mm, so that the whole crack front could be observed while maintaining a reasonable level of magnification. The bimaterial strip was made up of BK-7 glass and an epoxy, a modified bisphenol (Araldite GY502)‡ that was cured at room temperature with an amido-amine harder (HY955)‡. Surface preparation, molding and crack initiation procedures were the same as before, but the biaxial loading device was modified for the current study by adding two additional linear bearings in order to improve stiffness and also by incorporating an improved design for specimen alignment (Liang, 1993).

† A paper by Kendall (1991), noting the adhesive effect of electric fields across crack faces, was brought to the authors' attention after going to press.

‡ The supply of these materials by Ciba-Geigy, Inc. is gratefully acknowledged.

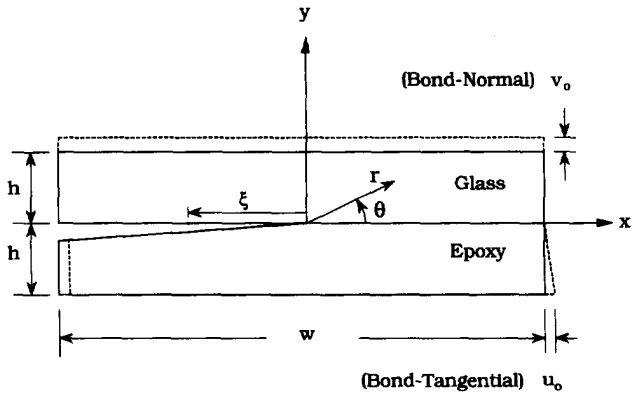

h = 0.95 cm
w = 17.8 cm
2b = 0.20 cm (specimen thickness)

Fig. 1. Geometry of the edge-cracked bimaterial strip specimen.

In the remainder of this section, we describe some extensions to crack opening interferometry that were made in order to provide more data and better error estimates for measurements close to the crack front. This is followed by a description of the manner in which cracks initiated and a presentation of the toughness values that were obtained from the interfacial fracture experiments.

2.1. *Normal crack opening displacement measurements*

Optical interferometry (Liechti, 1993) was used to measure the normal crack opening displacements (NCOD). A monochromatic light beam was introduced through the glass to the crack surfaces at normal incidence and the reflected beams were brought together by a microscope to form interference fringe patterns. The NCOD, δ, for a bright fringe of order m were determined through

$$\delta = m\lambda/2 \tag{1}$$

where λ was the wavelength of the incident light.

For the wavelength of light (546 nm) used in the experiments reported here, the resolution in NCOD from eqn (1) is 273 nm. This can be halved by considering dark and bright fringes. Further increases in resolution can be obtained by measuring the light intensity between fringes, as was done by Voloshin and Burger (1983) for photoelastic fringes. Although the analog version of the digital expression (1) can be applied to interpolate between fringes that are well removed from the crack front, modifications must be considered for interpolations near the crack front in order to account for refraction effects and larger crack opening angles.

The refraction effect essentially shifts the location of fringes and was first examined by Fowlkes (1975) who considered a crack in a homogeneous material under mode I loading. To simplify the calculation for our situation, we considered the case of a crack in glass under mode I loading. The variation of index of refraction, as suggested by Fowlkes, can be written as

$$n = n_0(1-\Delta) \tag{2}$$

where Δ is the dilatation, and n_0 is the index of refraction in the unstressed state. The equation for the path of a light ray passing through a medium having a variable index of refraction is

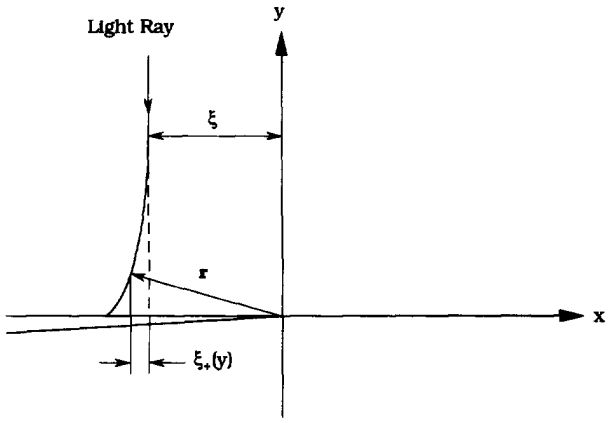

Fig. 2. Schematic for optical path deviation calculations.

$$\frac{\mathrm{d}}{\mathrm{d}s}\left(n\frac{\mathrm{d}\mathbf{r}}{\mathrm{d}s}\right)=\nabla n \tag{3}$$

where s is the optical path and $\mathbf{r}$ is the position vector of a point on the path as shown in Fig. 2. Consider a light ray that is initially parallel to the y axis and assume that, as the light ray approaches the crack tip region, there is a deviation $\xi_+(y)$ from the straight line. The position vector of a point on the light ray is $\mathbf{r}=-(\xi+\xi_+)\mathbf{i}+y\mathbf{j}$. Assuming that $\xi_+(y)$ is small, then the governing equation (3) becomes

$$\frac{\mathrm{d}}{\mathrm{d}y}\left(n\frac{\mathrm{d}\xi_+}{\mathrm{d}y}\right)+\frac{\partial n}{\partial x}=0. \tag{4}$$

The dilatation Δ is related to the stresses by

$$\Delta=\frac{1-2\nu}{E}\sigma_{kk}. \tag{5}$$

The governing equation (4) can then be solved with the following boundary conditions $\xi_+(\infty)=\xi'_+(\infty)=0$, where $\xi'_+\equiv \mathrm{d}\xi_+/\mathrm{d}y$. Using the material properties of glass (Table 1) and assuming an energy release rate $G=17.5\ \mathrm{J/m^2}$ (most severe mode I case), the error due

Table 1. Material properties

Material	Young's modulus E (GPa)	Poisson's ratio ν	Yield stress σ_0(MPa)	Hardening exponent n	Yield offset $\bar{\alpha}$
Epoxy	2.03	0.36	34.6	6	0.07
Glass	69.0	0.20	—	—	—

Ramberg–Osgood representation: $\varepsilon=\frac{\sigma}{E}+\bar{\alpha}\left(\frac{\sigma}{\sigma_0}\right)^{n-1}\frac{\sigma}{E}$

Epoxy/glass Dundurs' parameters $\alpha=-0.936$, $\beta=-0.188$
Bimaterial constant $\varepsilon=0.061$
$\omega(\alpha,\beta)$ $\omega=16.0^\circ$.

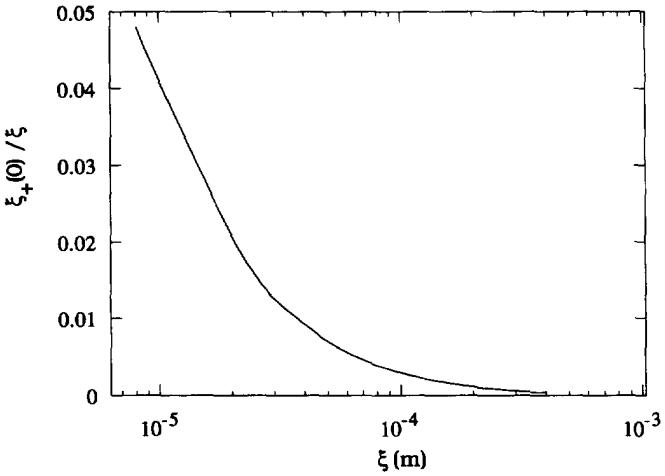

Fig. 3. Error estimate for the path deviation due to refraction.

to refraction was estimated as shown in Fig. 3. In the region where measurements were made ($\xi \geqslant 10^{-5}$ m), the error due to variations in the index of refraction was less than 4%. Therefore, for glass, the variation in index of refraction was a negligible source of error in locating the fringe peaks.

Another effect, which can significantly influence the measured NCOD near the crack front, is the reflection of light from crack faces with a large crack opening angle. A schematic diagram describing the geometric relation for the formation of interferometric patterns is shown in Fig. 4. The ray diagram in Fig. 4(a) is the classical one that is used for small wedge angles to obtain eqn (1) (Liechti, 1993). For larger crack opening angles closer to

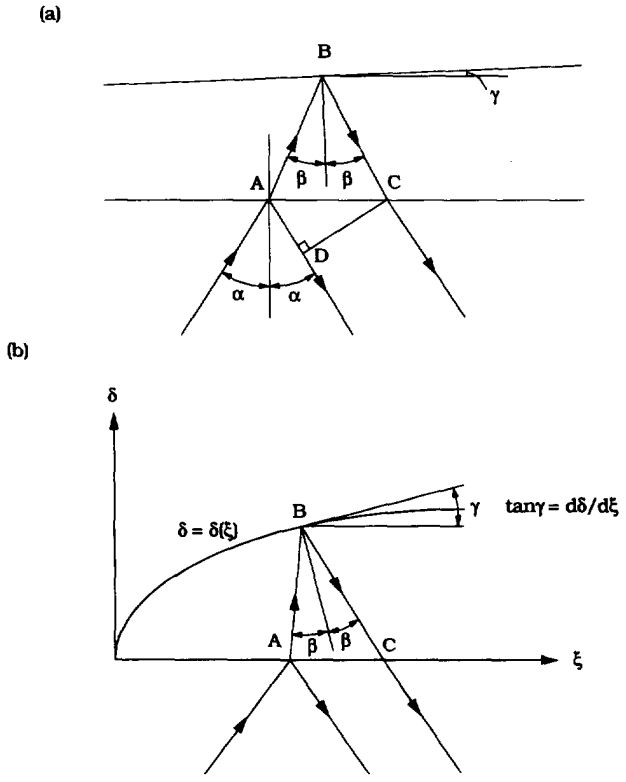

Fig. 4. Fringe formation for a crack with (a) small crack opening angle and (b) large crack opening angle.

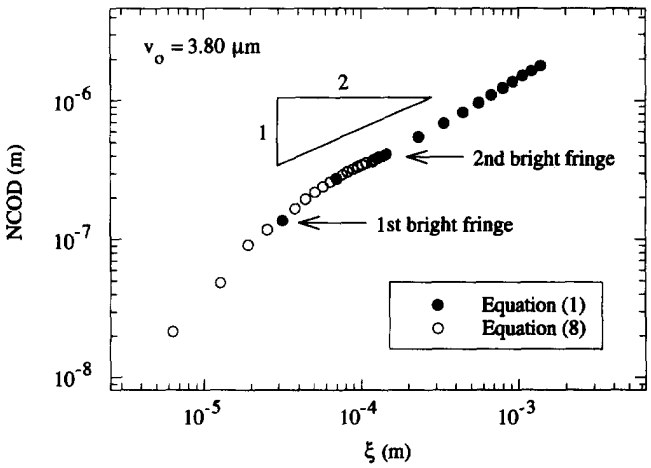

Fig. 5. NCOD ahead of the first and second order fringes.

the crack front, Fig. 4(b) was used. Assuming normal incidence, the actual NCOD, $\delta(\xi)$, are related to the light path difference δ_{LP} by

$$\delta_{LP} = \frac{2\delta}{1-\tan^2\gamma} \tag{6}$$

where $\gamma = \tan^{-1}(\mathrm{d}\delta/\mathrm{d}\xi)$. In order to obtain the actual NCOD, we rewrite (6) as

$$\frac{\mathrm{d}\delta}{\mathrm{d}\xi} = \sqrt{1-\frac{2\delta}{\delta_{LP}(\xi)}} \tag{7}$$

and solve it iteratively. Far from the crack front, the slopes are on the order of 0.01 radians or smaller, and the true NCOD can be obtained from (1). However, if we are interested in finding the NCOD ahead of the first order fringe, as will be discussed next, then the crack opening angle may be large and eqn (7) should be adopted.

An additional consideration is that eqn (1) has been used to obtain NCOD in an essentially digital manner from one fringe to another. The resolution in NCOD can be increased by measuring the variation in light intensity between fringes as has been suggested by Voloshin and Burger (1983) for photoelastic fringes. Considering normally incident light and using a wave representation, we can find (Liang, 1993) that

$$\sqrt{\frac{I}{I_p}} = \sin\left[\frac{\pi}{\lambda}\frac{2\delta}{1-(\delta')^2}\right] \tag{8}$$

where I is the intensity and I_p is the maximum intensity of the fringe patterns, and $\delta = \delta(\xi)$ is the actual distribution of the NCOD. The main implication of eqn (8) is that the NCOD ahead of the first order fringe can be determined, their resolution being limited only by that of the intensity measurement device. The scheme outlined above was applied to a cracked specimen under bond-normal loading. Interpolations (Fig. 5) were made between the crack front and the first and second order bright fringes. The consistency of the interpolations between the first and second order bright fringes established confidence in the results obtained close to the crack front where the NCOD decrease more rapidly than is suggested by $\sqrt{r}$ behavior. The measurements indicated that K-dominance lies between the first and second dark fringes. The additional drop in NCOD closer to the crack suggests that some relatively long range cohesive tractions are active.

2.2. *Experimental results*

The first aspect of the interface fracture experiments that was considered was three-dimensional effects. Based on previous experiments (Liechti and Knauss, 1982a, b) with a glass/polyurethane/glass sandwich, it was found that crack front shapes could change significantly with mode-mix. Recently, Jensen *et al.* (1990) in analysing the cut test, showed that the shape of the crack front was a complex interaction between stress state and mode I/II/III toughening effects. Thus, it was conceivable that in our experiments crack front shape could influence measured toughness values. In addition, the NCOD could vary significantly along the crack front. As was indicated earlier, the use of thinner specimens allowed the whole crack front to be observed during loading and crack initiation so that the issues raised above could be addressed.

Two typical crack front shapes are shown in Figs 6(a) and 6(b). The first arose when there was uniformly strong adhesion across the specimen thickness. The crack front was slightly concave in the direction of crack growth and the curvature of the front [Fig. 6(b)], was much greater, with the crack front leading considerably at the specimen edges. This was due either to a uniformly lower degree of adhesion or some weakness being introduced near the specimen edges during the specimen preparation. The effect of the second possibility is obvious but the first possibility is entirely consistent with the results of Jensen *et al.* (1990) who used crack front shapes to extract fracture toughness. For the straight crack fronts, the measured NCOD in the central region of the crack front were essentially independent [Fig. 7(a)] of through thickness location. On the other hand, curved crack fronts had a noticeable effect on the NCOD, as shown in Fig. 7(b), where the NCOD close to the free edge ($y/b = 0.9$) could be less than half the value in the central region of the specimen.

The process of crack initiation was quite complex in the sense that growth started at a random point on the crack front and spread laterally (i.e. along the crack front) before the whole crack front moved as a unit (self-similar growth). This was true for the cracks with relatively straight fronts as well as the curved ones. This had not been observed in previous experiments (Liechti and Chai, 1992), probably due to the fact that the adherends were beveled along the edges of the glass/epoxy interface, which pinned the crack front back at the edges (Liechti *et al.*, 1992). All subsequently presented results were obtained from cracks with straight fronts that grew in a self-similar manner after initiation.

The final step that was taken in assessing three-dimensional effects was to establish, for the 2.00 mm specimen thickness used here, whether plane strain or plane stress analyses could be used instead of three-dimensional ones. A detailed analysis of the three-dimensional stress distribution for an interface crack has recently been conducted by Lee and Rosakis (1993). For the specimens being considered here, the NCOD measurements for straight crack fronts were compared (Fig. 8) with solutions from plane stress, plane strain and three-dimensional analyses (Fig. 8) along the mid-thickness of the specimen for a purely bond-normal applied displacement. The plane stress and three-dimensional solutions were in closest agreement with the measurements for distances $\xi > 100$ μm from the crack front. Closer to the crack front, it can be seen that the measured NCOD drop sharply when compared to all the predictions. This point has already been noted in Fig. 5 and will be discussed later, but the close agreement between plane stress and three-dimensional analyses suggested that plane stress conditions would be sufficient for all subsequent analyses.

Based on the plane stress assumption, the fracture toughness was calculated from

$$G = \frac{1}{2h}\left[v_0^2\left(\frac{\tilde{E}_1\tilde{E}_2}{\tilde{E}_1+\tilde{E}_2}\right)+u_0^2\left(\frac{\mu_1\mu_2}{\mu_1+\mu_2}\right)\right] \tag{9}$$

where u_0 and v_0 are the applied displacement, μ_i are the shear moduli, $\tilde{E}_i = 2\mu_i/(1-\nu_i)$, ν_i are the Poisson's ratios, $i = 1$ for epoxy and $i = 2$ for glass. The results obtained in this way were compared (Fig. 9) with those from previous work (Liechti and Chai, 1992) where the specimen thickness was 6.35 mm instead of 2.00 mm. Closing or negative shear refers to the fact that loading in that direction tends to bring the crack faces closer together in

the crack front region. Opening or positive shear produces increases in NCOD near the crack front and closing near the crack mouth (Comninou and Schmueser, 1979; Liechti and Chai, 1991). Pure bond-normal loading resulted in a mode-mix of 0.1° based on a reference length of 100 μm. The toughness value obtained from this study under bond-normal loading was 7.8 J/m^2, about double the value that was determined previously (Liechti and Chai, 1992). The shape of the toughness distributions in the two studies also differed. In the experiments of Liechti and Chai (1992) the toughness was independent of mode-mix for $-25° \leqslant \psi \leqslant 45°$, whereas there was essentially no such behavior in the current experiments. The toughness distribution around the minimum value was much sharper this time and the minimum value did not occur at the mode-mix corresponding to bond-normal loading. It is not clear at this time whether or not the difference in toughness between the two sets of data was due to a difference in the intrinsic work of adhesion or the specimen thickness (plane stress vs plane strain). In any case, the difference in toughness distributions between the two sets of data is qualitatively consistent with predicted distributions (Tvergaard and Hutchinson, 1993) for increasing $\hat{\sigma}$, the maximum stress in the traction/separation law of the interface. The largest values of toughness were obtained with very small amounts of bond-normal displacements (less than 1 μm) growth. Pure shear experiments were attempted but crack initiation was catastrophic, usually branching into the epoxy for $\psi < 0$ and the glass for $\psi > 0$. The toughness value at $\psi = -52°$ was about 6 times the bond-normal value, and the crack initiation process was quite sudden compared to the gradual crack extension that occurred at lower values of $|\psi|$. Crack extension under positive shear occurred in a very characteristic stick–slip manner. This was in direct contrast to the mechanism that was observed under negative shear, where crack extension with time was very smooth and was accompanied by a lot of visible shearing (from the fringe patterns) of the material in the crack front region. Presumably this was due to the fact that, under high negative shear, the epoxy in the crack front region is being compressed towards the interface and the only degree of freedom is shearing.

By comparing the toughness curves generated by the embedded process zone approach [Fig. 8(a), Tvergaard and Hutchinson, 1993] and Fig. 9 of this paper we can examine the bounds for the separation law that might apply to the glass/epoxy interface being considered. The $\hat{\sigma}/\sigma_y = 1.4$ curve from the analysis corresponds to the toughness curve of the thicker specimens, whereas $\hat{\sigma}/\sigma_y = 2.4$ more closely follows the toughness distribution of the thinner specimens. The toughness of the thin and thick specimens at $\psi = 0$ was 7.8 and 3.3 J/m^2, respectively. Especially for $\hat{\sigma}/\sigma_y = 1.4$, it can be seen that $G_c = \Gamma_0$, the work of separation. Thus if we take $\Gamma_0 = 5$ J/m^2, we find from eqn (1.4) of Tvergaard and Hutchinson (1993) that the maximum separation δ_n^c is of the order of 0.1 μm for an epoxy yield strength of 30 MPa. Such NCOD are on the boundary of the resolution of the crack opening interferometry measurements in going from dark to bright fringes. The higher resolution provided by interpolation between fringes (8) leads to resolution of NCOD of the order of 0.02 μm (Fig. 5). Although the result in Fig. 5 suggests that δ_n^c should be less than 0.02 μm for this interface, the applied displacement level was not critical, so that the maximum separation of the interface would not yet have been excited. At the critical applied displacement levels and the magnifications used for these experiments, it was not always possible to resolve the first and second bright fringes (Figs 10–12) so that $\delta_n^c \sim 0.1$ μm are certainly feasible.

3. ANALYSIS AND DISCUSSION

The stress analyses that were used to examine various potential toughening mechanisms were made with the finite element code ABAQUS†. Several stress/strain laws were considered for the epoxy, including linearly elastic, rate independent and rate dependent plasticity responses. The parameters for these models were obtained from uniaxial tension, plane strain compression, and combined normal and shear stress experiments at various rates (Liang, 1993). The rate independent plasticity analyses that were conducted were

† We are grateful to Hibbit, Karlsson and Sorensen, Inc. for making ABAQUS available under an academic license.

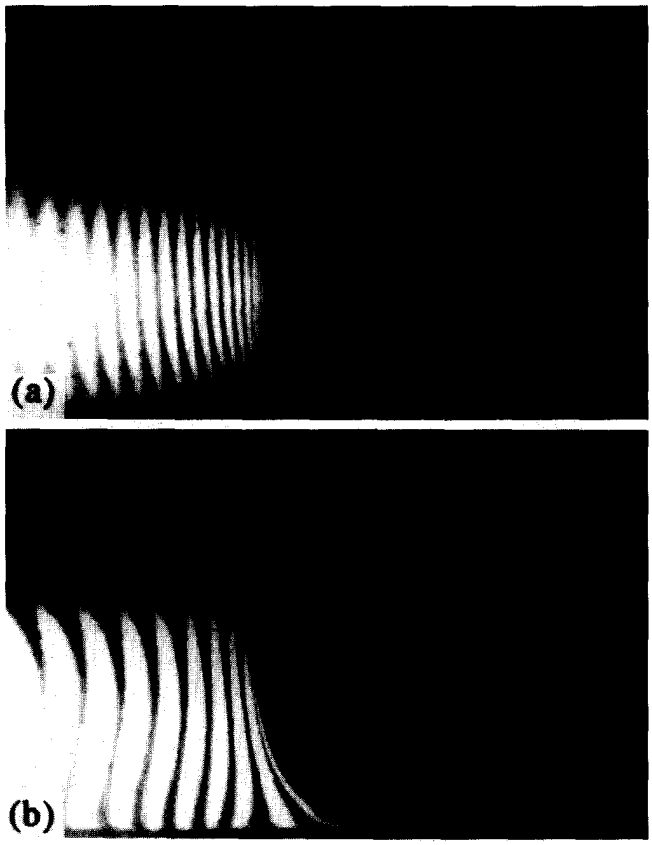

Fig. 6. Photographs of starter cracks; (a) straight crack, (b) curved crack.

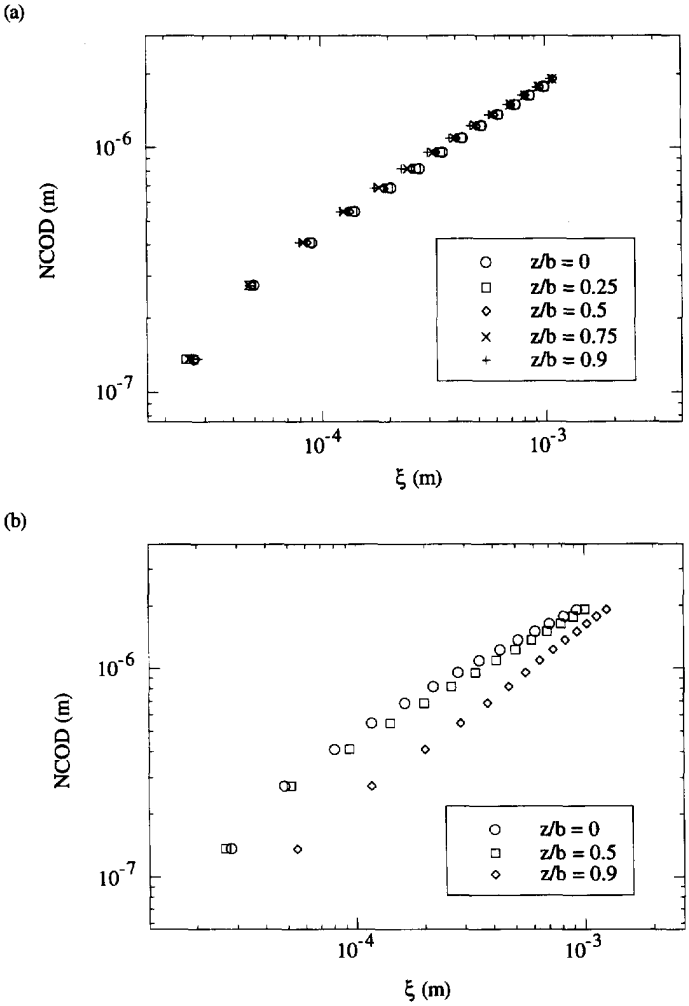

Fig. 7. Thickness distribution of the NCOD associated with (a) straight crack front, (b) curved crack front.

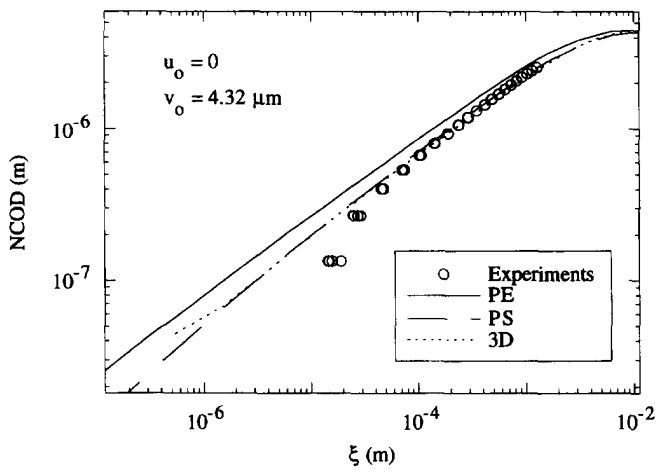

Fig. 8. Comparison of measured NCOD with plane stress (PS), plane strain (PE) and three-dimensional (3D) analyses.

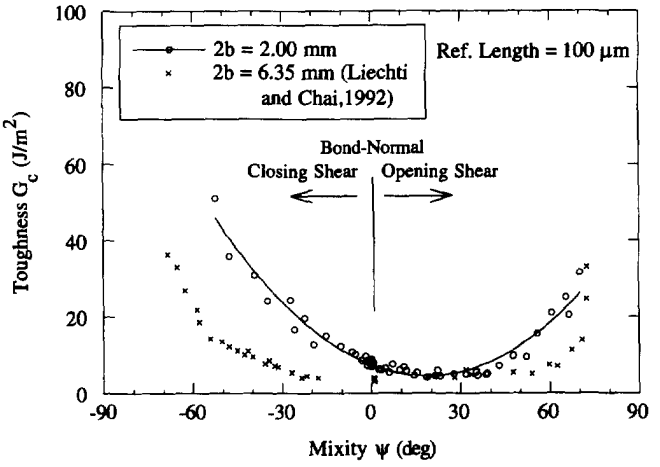

Fig. 9. Variation of interfacial toughness with mode-mix for two specimen thicknesses.

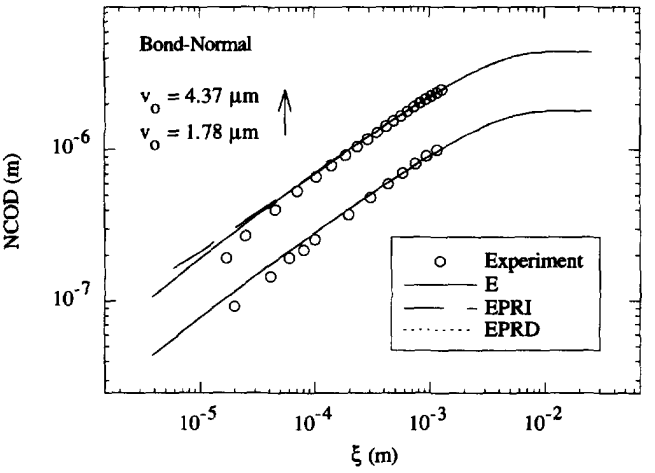

Fig. 10. Comparison of measured NCOD with elastic (E), rate independent plasticity (EPRI) and rate dependent plasticity (EPRD) predictions for bond-normal loading.

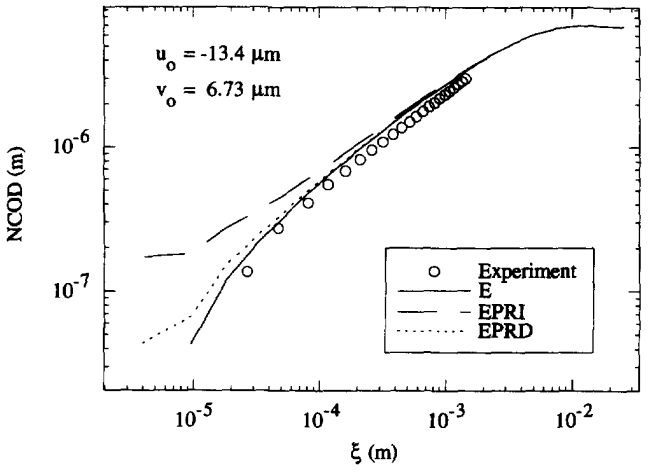

Fig. 11. Comparison of measured NCOD with elastic (E), rate independent plasticity (EPRI) and rate dependent plasticity (EPRD) predictions for negative shear loading.

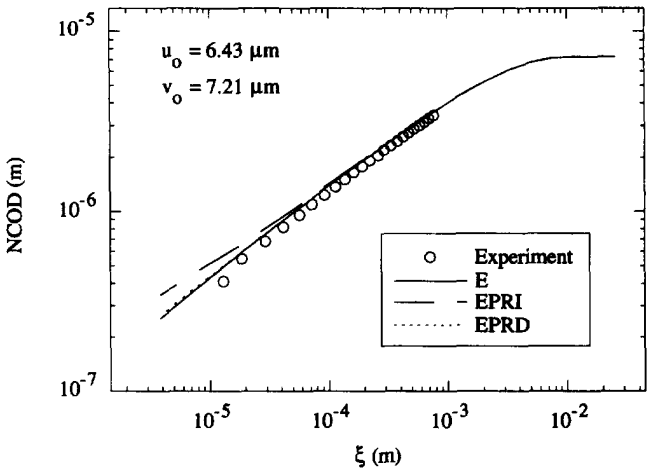

Fig. 12. Comparison of measured NCOD with elastic (E), rate independent plasticity (EPRI) and rate dependent plasticity (EPRD) predictions for positive shear loading.

mainly J_2-deformation theory analyses. The results from such analyses were designated as EPRI in Figs 10–12. The rate dependent flow rule that was incorporated in the finite element analyses had the form

$$\dot{\bar{\varepsilon}}^{\mathrm{p}} = D\left(\frac{\sigma_{\mathrm{y}}}{\sigma_0} - 1\right)^q \tag{10}$$

where $\dot{\bar{\varepsilon}}^{\mathrm{p}}$ is the rate of equivalent plastic strain, σ_{y} is current yield stress, σ_0 is the quasi-static yield stress, and D and q are material properties that were obtained from various constant strain rate, pure shear experiments (Liang, 1993). The results obtained from these analyses were designated EPRD in Figs 10–12. The NCOD were measured during all the mixed-mode fracture experiments whose toughness values were presented in Fig. 9. The measured values are now compared with predictions based on the different constitutive behaviors described above for cases involving pure bond-normal and shear dominant (positive and negative) loadings.

The first comparisons are made (Fig. 10) for two levels of bond-normal loading, with the NCOD values between the crack front and the first bright fringe having been interpolated from (8). For the lower load level ($v_0 = 1.78$ μm), the nonlinear (EPRI, EPRD) and linear solutions were the same in the domain being examined and reasonably matched the measured values far from the crack front. However, the measured values were noticeably lower near the crack front. At the higher load level ($v_0 = 4.37$ μm), there were signs of blunting when the EPRI and linear solutions were compared. The EPRD results indicated that no blunting should occur, as they were in agreement with the NCOD from the elastic prediction. Neither solution really matched the measured NCOD near the crack front, which were noticeably smaller.

The differences noted above for bond-normal loading were greater when a bond normal loading was added sequentially to a shear load. The differences were greatest for negative shears (Fig. 11) where the EPRI analysis predicted a large degree of blunting. A smaller degree of crack tip blunting was predicted by the EPRD model. Again, it was evident that the measured NCOD were even lower than the values obtained from the elastic analysis. Similar but smaller differences were apparent for positive shear as shown in Fig. 12. The consistently higher values of predicted NCOD suggested that relatively long range cohesive stresses could be acting on the crack faces, as will be discussed later.

One of the reasons for conducting the elastoplastic analyses was to be able to determine the amount of plastic dissipation associated with crack initiation and stable growth. An estimate was made based on the analyses of stationary cracks and the crack length independence of the fracture parameters in the specimen. The plastic zone shapes associated

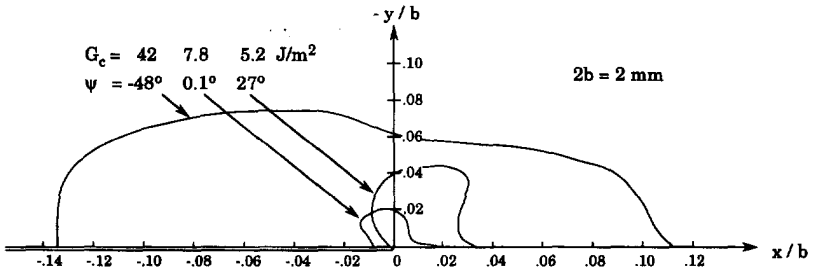

(a) Plastic zone shapes as a function of mode-mix

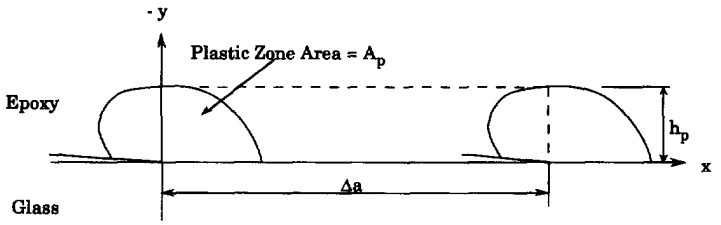

(b) Schematic for plastic dissipation calculations

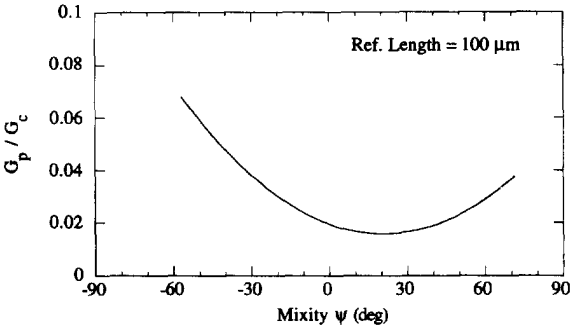

(c) Plastic dissipation as a function of mode-mix

Fig. 13. Plastic zone shapes and dissipation.

with the critical applied displacement levels in the three examples considered in Figs 10–12 were determined on the basis of the rate independent plasticity analyses [Fig. 13(a)]. While yielding was clearly small scale in nature, its extent varied considerably, with the biggest difference arising between the nominally mode I result and the negative shear at $\psi = -48°$. If we let W_p be the plastic dissipation associated with each plastic zone having area A_p at critical load then

$$W_p = \int_{A_p} W \, dA_p \tag{11}$$

where W is the dissipation density $W(x, y) = \int \sigma \cdot d\varepsilon^p$. W_p was calculated using a post processing routine in ABAQUS. An average dissipation density $\bar{W}$ was defined as

$$\bar{W} \equiv \frac{W_p}{A_p}. \tag{12}$$

Since the edge-cracked bimaterial strip is a steady state specimen, the plastic zone size is independent of crack length for a constant load. We saw from the experiments that the

crack growth was self-similar in crack front geometry and NCOD during a crack extension Δa. As a result, the plastic dissipation due to the crack extension is simply

$$W_{\Delta a} \approx \bar{W} h_p \Delta a \tag{13}$$

where h_p is the height of the plastic zone, and $(h_p \Delta a)$ is the area of plastically deformed material that is swept out [Fig. 13(b)] during the crack extension. The plastic component G_p of the total toughness G_c is then

$$G_p \equiv \frac{W_{\Delta a}}{\Delta a} = \frac{W_p h_p}{A_p}. \tag{14}$$

Thus, the plastic component G_p can be calculated from the known plastic zone area A_p, its height h_p, and the associated dissipation W_p. This approach allows us to estimate the plastic dissipation component but ignore the energy stored in the wake, which was shown to be small even for the tough material considered in the work of Shivakumar and Crews (1987). An interesting point from (14) is that the plastic dissipation component is a shape sensitive quantity; that is, G_p is proportional to the ratio of h_p/A_p.

Using (14), we were able to calculate the plastic dissipation component G_p for each of the crack initiation experiments that were conducted. The ratio of G_p/G_c [Fig. 13(c)] for all the mode-mixes ranged from 1.5% to 7.0%. The analysis by Tvergaard and Hutchinson (1993) showed that the ratio of G_p/G_c ranged from 14% (at $\psi = 0°$) to 87% (at $\psi = 40°$) for $\delta_n^c/\delta_t^c = 1$ and a maximum cohesive stress to yield stress ratio $\hat{\sigma}/\sigma_y = 2.0$. Thus it is possible that interfacial toughening due to increase in plastic dissipation with shear can occur. However, without a specific traction/separation law for the glass/epoxy interface, it is not clear yet whether or not the low G_p/G_c values obtained from the approximate analysis of stationary cracks that was conducted here is valid. However, in light of the fact that the rate dependent plasticity model brought the predicted and measured NCOD into closer agreement, and also because there was no sign of large scale yielding, it is certainly possible that plastic dissipation was small here. Using the analysis of Drugan *et al.* (1982) for steadily growing cracks in homogeneous materials, the parameter ρ in their model was found to be 1×10^{-7} m using the NCOD in Fig. 10, and the corresponding steady state J-integral was 0.096 J/m^2, which was 1.2% of G_c at $\psi = 0°$. As can be seen from Fig. 13(b), the corresponding percentage from the stationary crack analysis was 2%, suggesting that a reasonable estimate was made and that plastic dissipation in these glass/epoxy specimens was indeed small.

The possibility of asperity shielding (Evans and Hutchinson, 1989) had been previously (Liechti and Chai, 1992) examined for this glass/epoxy interface. Due to the fine polishing that the glass was given and the clean crack faces prior to and following the fracture, asperities did not give rise to any appreciable shielding in these experiments (Liang, 1993).

The measured NCOD in Figs 10–12, showed a clear departure from elastic and elastoplastic analysis close to the crack front. In addition, the departure was not due to blunting, as might be expected, but in the opposite direction; near the crack front the NCOD were always lower than even the elastic predictions. These results and the observations of Zimmerman *et al.* (1991) and Horn and Smith (1992) motivated an examination of electrostatic effects on NCOD. The results of the examination are preliminary but should encourage further work. The first step that was taken was to grow a crack, arrest it (without crack face contact) and then apply a cyclic bond-normal loading and unloading that produced crack face contact during unloading and produced no further crack growth during the loading portion. The measured NCOD from three series of experiments are shown in Figs 14(a–c) where the NCOD, normalized by the applied bond-normal displacement, are plotted as a function of distance from the crack front, for zero contact and various numbers

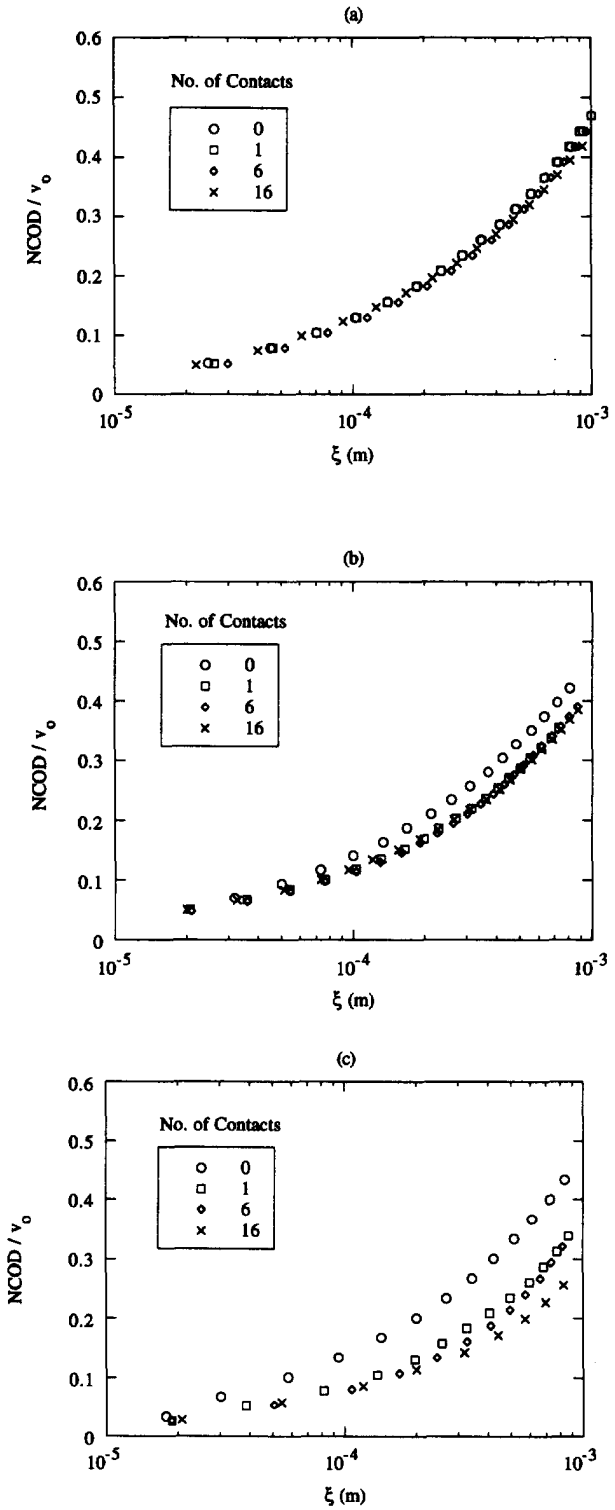

Fig. 14. NCOD/v_0 for various contact times in three series of experiments.

of subsequent contacts. In the first case [Fig. 14(a)], there was no effect of subsequent crack face contact. In the second case [Fig. 14(b)], there was a difference between the NCOD profile after zero contact and all subsequent contacts which did not, however, differ from one another. In the third case [Fig. 14(c)], the number of contacts appeared to have an effect on the NCOD. It is not entirely clear why the responses shown in Figs 14(a) and 14(b) differ. It is possible that discharging occurred in the first case but not the second, due

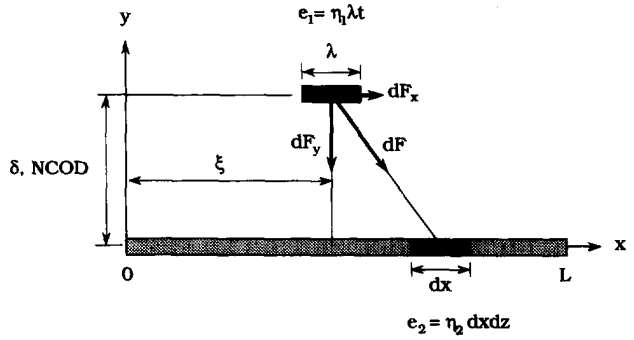

Fig. 15. Schematics for electrostatic stress calculations.

to differences in environmental conditions. These will have to be more carefully controlled in the future. In the third case [Fig. 14(c)], some experiments with sliding contact were conducted between the noted experiments and may have caused additional charging. Clearly this interesting possibility needs to be considered more carefully.

The possibility that electrostatic effects were causing the lower NCOD near the crack front was explored by conducting two analyses. First an electrostatic traction vs NCOD law was developed by integrating Coulomb's law for the force between point charges. The charge density was left as a free parameter. The second (finite element) analysis used the difference between measured and predicted NCOD to extract the tractions along the crack faces. The two traction vs NCOD laws were then compared in order to establish the charge density that was needed. The details now follow.

The electrostatic force between two point charges is governed by Coulomb's law, which has the following form

$$F = \frac{k e_1 e_2}{d^2} \tag{15}$$

where F is the electrostatic force, e_1 and e_2 are the electrical charges, d is the distance separating the point charges, and $k = 1/4\pi\varepsilon_0$ (8.99×10^9 m/F). In Fig. 15, an elemental section λt (λ in x and t in z) of the top crack face with a charge density η_1 will observe an electrostatic force

$$\mathrm{d}F = \frac{k\eta_1\eta_2 \lambda t \,\mathrm{d}x\,\mathrm{d}z}{(x-\xi)^2 + \delta^2 + (z-\xi)^2} \tag{16}$$

from a differential section $(\mathrm{d}x)(\mathrm{d}z)$ on the bottom crack face with a charge density η_2. The total force F is calculated simply by integrating (16) along the whole effective charge area $L \times 2B$ (L and $2B$ are the effective charge lengths in x and z). The tractions on the crack surface are then

$$T_y = \frac{F_y}{\lambda t} = k\eta_1\eta_2 \left\{ \tan^{-1}\left[\frac{z(L-\xi)}{\delta\sqrt{(L-\xi)^2+\delta^2+z^2}}\right] + \tan^{-1}\left[\frac{z\xi}{\delta\sqrt{\xi^2+\delta^2+z^2}}\right]\right\}_{z=-B-\zeta}^{z=B-\zeta} \tag{17}$$

and

$$T_x = \frac{F_x}{\lambda t} = k\eta_1\eta_2 \ln\left[\frac{z+\sqrt{\xi^2+\delta^2+z^2}}{z+\sqrt{(L-\xi)^2+\delta^2+z^2}}\right]_{z=-B-\zeta}^{z=B-\zeta} \tag{18}$$

where the charge densities η_1 and η_2 are assumed to be constant. For locations near the crack tip, we have $\delta \ll \xi \ll L$, and at the specimen center, we have $\zeta = 0$, so that (17) and (18) can be further simplified to

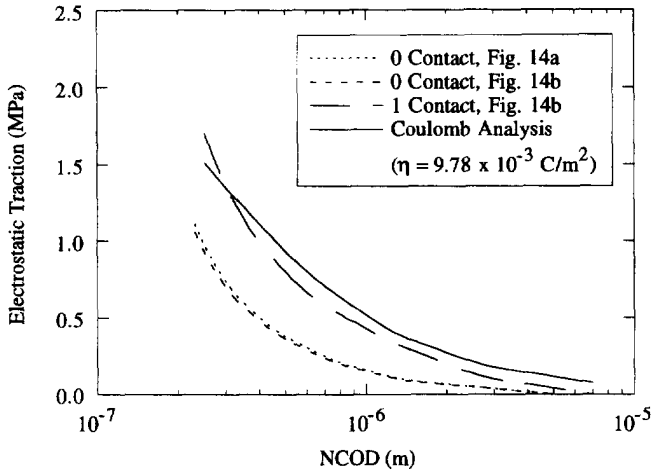

Fig. 16. Electrostatic traction as a function of NCOD.

$$T_y = 2k\eta_1\eta_2 \tan^{-1}\left(\frac{B}{\delta}\right) \quad \text{and} \quad T_x \approx 0 \tag{19}$$

which indicate that the electrostatic stresses are strongly mode I dominant.

The distribution of surface tractions was also determined by using the differences between the measured NCOD and the values predicted by the rate dependent plasticity analyses. The rate dependent analysis was first conducted, subject to the applied displacements that were recorded during the crack initiation experiments. This resulted in the differences in NCOD such as those that are shown in Figs 10–12. The NCOD were brought into agreement in a separate analysis where the globally applied displacements and the difference in NCOD along the crack faces were applied at the same rate. In spite of the nonlinear material behavior and the coupling between crack face tractions and NCOD, this simple superposition resulted in agreement between measured and predicted NCOD without any iteration. The required tractions were then obtained from the reactions along the portions of the crack faces where NCOD had originally differed.

The tractions derived from Coulomb's law and the finite element analyses are compared in Fig. 16, in a plot of tractions vs NCOD. The broken lines are from the finite element analysis for two cases where no contact had occurred [Figs 14(a, b)] and one case where one contact had occurred [Fig. 14(b)]. The results of a Coulomb analysis (19) with an equal charge density of 9.78×10^{-3} C/m^2 on the glass and epoxy crack faces are shown as the full line, which was quite close to the single contact case. The distribution for the zero contact cases in Fig. 16 could be matched by using a charge density of 7.3×10^{-3} C/m^2 (Liang, 1993). Such charge densities appear to be high for polymers. For example, the typical charge density for a polyethylene/metal interface in air is 5×10^{-5} C/m^2 (Lowell and Rose-Innes, 1980). However, Horn and Smith (1992) also noted higher charge densities in their work. It is also interesting to note that the tractions for a given NCOD were higher following contact, suggesting that it had produced additional charging, as noted by Horn and Smith (1992). Of course, the association of the tractions with electrostatic effects in this study is indirect in the sense that no measurements of charging were made. Nonetheless, the NCOD measurements definitely indicate that long range tractions were active along the crack faces, whatever their origin may have been.

The question then arises as to how much shielding was provided by the long range tractions. The calculation was made by making use of a judicial choice of J-integral contours. With the J-integral defined as

$$J = \int_\Gamma \left(W\,\mathrm{d}y - \mathbf{T} \cdot \frac{\partial \mathbf{u}}{\partial x}\,\mathrm{d}s \right) \tag{20}$$

the contribution associated with the tractions was obtained by choosing two contours; one

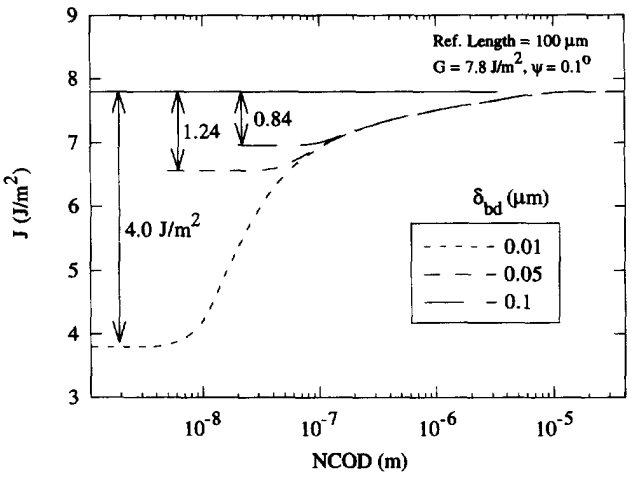

Fig. 17. The contribution of crack face tractions to the J-integral.

outside the zone where tractions were applied and the other very close to the crack tip. The presence of nonzero tractions on the crack faces gives rise to a nonzero contribution to J which is the shielding provided by the tractions. Thus, the shielding value of J is

$$J_s = \int_b^a T_y(\xi) \frac{\partial \delta}{\partial \xi} \, d\xi \tag{21}$$

where a is the distance from the crack where the tractions become zero for large NCOD ($\sim 10^{-5}$ m in Fig. 16) and b is a location close to the crack front where breakdown must occur due to charge neutralization. For convenience at this stage, we will consider that b is greater than any process zone, such as a Barenblatt cohesive zone that governs the intrinsic adhesion of the interface. For fixed applied displacements, the NCOD are some function of the distance from the crack front so that the variation of shielding within the shielding zone is

$$\tilde{J}_s(\delta) = \int_{\delta(\xi = a)}^{\delta} T_y(\hat{\delta}) \, d\hat{\delta} \tag{22}$$

where δ is the NCOD at some point in $b \leqslant \xi \leqslant a$. The integration (22) was carried out for a bond-normal loading ($\psi = 0.1°$) with $G = 7.8$ J/m^2. The separation law $T_y(\delta)$ that was used was the zero contact case in Fig. 16 extrapolated to $\delta = 0.1$, 0.05, 0.01 μm, and then taken to be zero thereafter, effectively making $\delta = 0.1$, 0.05, 0.01 μm, respectively, the NCOD at breakdown. The result is shown in Fig. 17 where J drops from the global G level (7.8 J/m^2) to values of 6.96, 6.56, 3.8 J/m^2 after charge neutralization. The shielding J_s (G_{es}) provided by the tractions is the difference between the two levels and can be seen in Fig. 17. The importance of determining the breakdown distance is clear as can be seen from the resulting difference in shielding. If the breakdown NCOD were greater than 0.05 μm, then there was not much sensitivity to them. However, breakdown NCOD of the order of 0.01 μm led to significant shielding levels. Clearly, higher resolution measurements of NCOD are required to resolve this issue. Another point to note is that if J-integral values could be determined entirely from measurements along several paths that included the traction zone, then the tractions could be determined by taking derivative of (22) so that

$$T_y = \frac{d\tilde{J}_s}{d\delta} \tag{23}$$

as has been recently suggested by Kim (1993) for dislocations. The inverse approach used

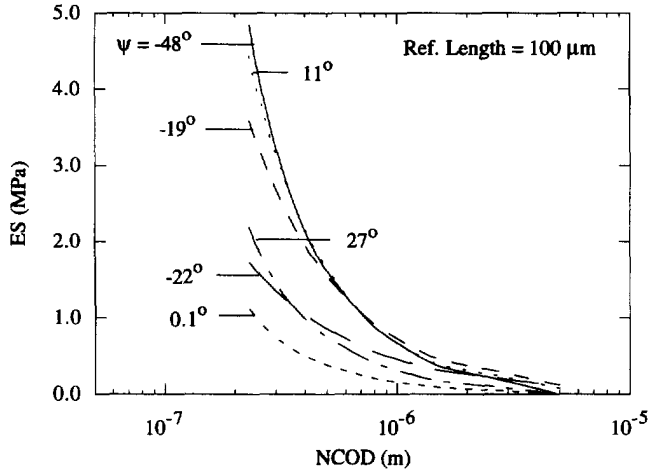

Fig. 18. Traction/separation laws generated under various mixed-mode conditions.

by Ungsuwarungsri and Knauss (1987) for obtaining separation law for softening materials is another possibility.

The procedure that was used to generate the traction/separation laws (Fig. 16) was used to generate similar laws for a number of the crack initiation experiments. The differences between the rate dependent plasticity analyses and the measured NCOD (such as those that appeared in Figs 10–12) gave rise to the traction/separation laws shown in Fig. 18. The distributions were a function of mode-mix, with a negative mode-mix generating the highest tractions for a given NCOD, perhaps due to the sliding frictional contact that is generated near the crack front during a portion of the loading.

The corresponding shielding values were determined by applying eqn (22) with a breakdown NCOD of 0.1 μm. The results exhibited a large degree of scatter when plotted as a function of mode-mix (Fig. 19). The normalized values of G_{es} exhibited a gradual rise from negative shear to positive shear, which did not follow the U-shaped distribution of toughness vs mode-mix. There could be several reasons for the scatter, such as variation in humidity and surface toughness (of the order of nanometers). These certainly call for a series of experiments where humidity is carefully controlled such as *in vacuo*. However, nanoscale fracture surface roughness may be hard to avoid and could cause problems if breakdown NCOD are of the same order. The choice of 0.1 μm as the NCOD at which breakdown occurred led to shielding levels that ranged from 10 to 40% and, as discussed earlier (Fig. 17), represent a lower bound. Thus if electrostatic effects were indeed contributing to the long range cohesive tractions that were observed, they could provide a significant degree of shielding.

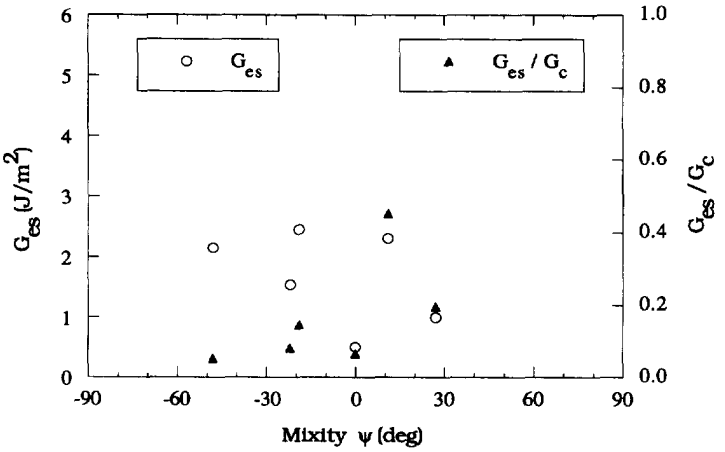

Fig. 19. Electrostatic shielding as a function of fracture mode-mix.

4. CONCLUSIONS

A series of mixed-mode interfacial crack initiation experiments were conducted using glass/epoxy bimaterial edge-cracked strip specimens under biaxial loading. The specimens were thinner than those that were used in a previous set of experiments so that three-dimensional effects could be examined and, to a certain extent, controlled by observation of the whole crack front. The thinner specimens exhibited higher toughness values and a different toughness vs mode-mix distribution. Three-dimensional effects due to variation in crack front geometry with mode-mix were effectively ruled out by only making use of data from specimens in which crack fronts were straight over about 90% of the specimen thickness. This allowed other toughening mechanisms to be considered through comparisons between NCOD that were measured using optical interferometry and predictions that were based on rate dependent and independent plasticity analyses.

Although the measured NCOD and all predictions were in agreement far from the crack front, the measured NCOD consistently fell below even the linear analyses near the crack front. The lower NCOD were ascribed to the presence of long range cohesive tractions acting on the crack faces, possibly due to electrostatic effects. The long range tractions provided a larger degree of shielding than either plastic dissipation or asperity shielding for the conditions and materials that applied in this study. Closer control of environmental effects are expected to reduce the scatter in the examination of electrostatic effects while the development of a separation law for the glass epoxy interphase region will allow the viscoplastic dissipation associated with initiation to be extracted in a more rigorous fashion.

Acknowledgments—The authors would like to acknowledge the financial support that was provided by the Office of Naval Research (N00014-90-J-4024) and the National Science Foundation (MSS-9201929).

REFERENCES

Cao, H. C. and Evans, A. G. (1989). An experimental study of the fracture resistance of bimaterial interfaces. *Mech. Mater.* **7,** 295–304.

Comninou, M. and Schmueser, D. (1979). The interface crack in a combined tension–compression and shear field. *J. Appl. Mech.* **46,** 345–348.

Drugan, W. J., Rice, J. R. and Sham, T.-L. (1982). Asymptotic analysis of growing plane stain tensile crack in elastic–ideally plastic solids. *J. Mech. Phys. Solids* **30,** 447–473.

Evans, A. G. and Hutchinson, J. W. (1989). Effects of non-planarity on the mixed mode fracture resistance of bimaterial interfaces. *Acta Metall. Mater.* **37,** 909–916

Fowlkes, C. W. (1975). Crack opening interferometry—the effects of optical refraction. *Engng Fract. Mech.* **7,** 689–692.

Horn, R. G. and Smith, D. T. (1992). Contact electrification and adhesion between dissimilar materials. *Science* **256,** 362–364.

Jensen, H. M., Hutchinson, J. W. and Kim, K.-S. (1990). Decohesion of a cut prestressed film on a substrate. *Int. J. Solids Structures* **26,** 1099–1114.

Kendall, K. (1991). Adhesive effects of electric fields across cracks. *J. Phys. D: Appl. Phys.* **24,** 1072–1075.

Kim, K.-S. (1993). Private communication.

Lee, Y. J. and Rosakis A. J. (1993) Interfacial cracks in plates: a three-dimensional numerical investigation. *Int. J. Solids Structures* **30,** 3139–3158.

Liang, Y.-M. (1993). Toughening mechanisms in mixed-mode interfacial fracture. Ph.D. Dissertation and *Engineering Mechanics Research Laboratory Report EMRL* #93/12, The University of Texas at Austin.

Liechti, K. M. (1993). On the use of classical interferometry techniques in fracture mechanics. In *Experimental Techniques in Fracture* (Edited by J. S. Epstein), Chapter 4. VCH Publishers, NY.

Liechti, K. M. and Chai, Y.-S. (1991). Biaxial loading experiments for determining interfacial toughness. *J. Appl. Mech.* **113,** 680–687.

Liechti, K. M. and Chai, Y.-S. (1992). Asymmetric shielding in interfacial fracture under in-plane shear. *J. Appl. Mech.* **59,** 295–304.

Liechti, K. M. and Hanson, E. C. (1988). Nonlinear effects in mixed-mode interfacial delaminations. *Int. J. Fract.* **36,** 199–217.

Liechti, K. M. and Knauss, W. G. (1982a). Crack propagation at material interfaces. I. Experimental technique to determine crack profile. *Expl Mech.* **22,** 262–269.

Liechti, K. M. and Knauss, W. G. (1982b). Crack propagation at material interfaces. II. Experiments on mode interaction. *Expl Mech.* **22,** 383–391.

Liechti, K. M. and Liang, Y.-M. (1992). The interfacial fracture characteristics of bimaterial and sandwich blister specimens. *Int. J. Fract.* **55,** 95–114.

Liechti, K. M. and Shirani, A. (1994). Large scale yielding in blister specimens. *Int. J. Fract.* **67,** 21–36.

Liechti, K. M., Chai, Y.-S. and Liang, Y.-M. (1992). Three dimensional effects in interfacial crack propagation. *Expl Mech.* **32,** 218–224.

Lowell, J. and Rose-Innes, A. C. (1980). Contact electrification. *Adv. Physics* **29,** 947–1023.

O'Dowd, N. P., Stout, M. G. and Shih, C. F. (1991). Fracture toughness of alumina–niobium interfaces: experiments and analyses. *Phil. Mag.* **A66,** 1037–1064.

Sharpe, L. H. (1972). The interphase in adhesion. *J. Adhesion* **4,** 51–64.

Shivakumar, K. N. and Crews, J. H., Jr (1987). Energy dissipation associated with crack extension in an elastic–plastic material. *Engng Fract. Mech.* **28,** 319–330.

Thouless, M. D. (1990). Fracture of a model interface under mixed-mode loading. *Acta. Metall. Mater.* **38,** 1135–1140.

Thurston, M. E. and Zehnder, A. T. (1993). Experimental determination of silica/copper interfacial toughness. *Acta Metall. Mater.* **41,** 2985–2992.

Tvergaard, V. and Hutchinson, J. W. (1992). The relation between crack growth resistance and fracture process parameters in elastic–plastic solids. *J. Mech. Phys. Solids* **40,** 1377–1397.

Tvergaard, V. and Hutchinson, J. W. (1993). The influence of plasticity on mixed mode interface toughness. *J. Mech. Phys. Solids* **41,** 1119–1135.

Ungsuwarungsri, T and Knauss, W. G. (1987). The role of damage-softened material behavior in the fracture of composites and adhesives. *Int. J. Fract.* **35,** 221–241.

Voloshin, A. and Burger, C. P. (1983). Half fringe photoelasticity: a new approach to whole field stress analysis. *Expl Mech.* **23,** 304–313.

Wang, J.-S. and Suo, Z. (1990). Experimental determination of interfacial toughness curves using Brazil-nut-sandwiches. *Acta. Metall. Mater.* **38,** 1279–1290.

Zimmerman, K. A., Langford, S. C. and Dickinson, J. T. (1991). Electrical transients during interfacial debonding and pullout of a metal rod from an epoxy matrix. *J. Appl. Phys.* **70,** 4808–4815.